

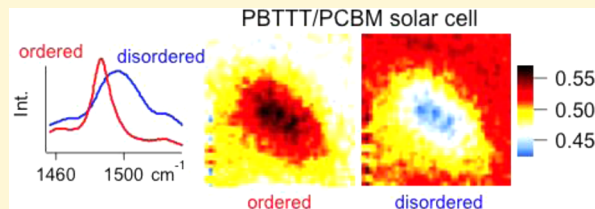
Spatially Resolving Ordered and Disordered Conformers and Photocurrent Generation in Intercalated Conjugated Polymer/Fullerene Blend Solar Cells

Jian Gao, Alan K. Thomas, Ryan Johnson, Hua Guo, and John K. Grey*

Department of Chemistry and Chemical Biology, University of New Mexico, Albuquerque, New Mexico 87131, United States

Supporting Information

ABSTRACT: Resonance Raman spectroscopy was used to identify ordered and disordered conformers of poly(2,5-bis(3-tetradecylthiophen-2-yl)thieno[3,2-*b*]thiophene) (PBT TT) blended with the electron acceptor [6,6]-phenyl C₆₁ butyric acid methyl ester (PCBM) in bulk heterojunction (BHJ) solar cells where PCBM intercalates into PBT TT side groups. We show that the PBT TT thiophene ring symmetric C=C stretching mode consists of contributions from ordered ($\hbar\omega_{C=C} = 1489 \text{ cm}^{-1}$, fwhm $\sim 15 \text{ cm}^{-1}$) and disordered ($\hbar\omega_{C=C} = 1500 \text{ cm}^{-1}$, fwhm $\sim 25 \text{ cm}^{-1}$) components and their relative amounts are sensitive to PCBM loading, annealing and excitation energy. The 1500 cm⁻¹ PBT TT component originates from twisted thiophene rings and disordered side groups due to PCBM intercalation in a mixed kinetic phase and thermal annealing promotes ordering of PBT TT chains from the formation of bimolecular PBT TT/PCBM crystals. Density functional theory (DFT) Raman simulations of PBT TT monomers support these assignments. Resonance Raman images of annealed PBT TT/PCBM model solar cells confirm that ordered PBT TT chains are most concentrated in PCBM-rich bimolecular crystals and corresponding intensity modulated photocurrent spectroscopy (IMPS) and imaging measurements show increased nongeminate charge recombination at the boundaries of ordered/disordered regions.

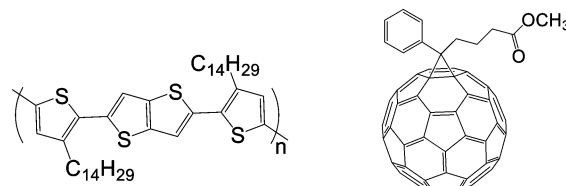


1. INTRODUCTION

The degree of mixing of fullerene acceptors with conjugated polymer donors used for thin film BHJ solar cells has significant implications for determining morphologies and overall device performance.^{1,2} Blends of PBT TT and PCBM are an ideal BHJ system for understanding how molecular mixing influences the outcomes of photovoltaic processes.^{3–5} PBT TT chains readily assemble into well-ordered π -stacked lamellar crystalline structures,⁶ essential for establishing multidimensional charge and energy transfer pathways. Extensive X-ray scattering and diffraction,^{5–9} solid-state NMR spectroscopy,⁵ differential scanning calorimetry (DSC),³ and IR spectroscopy studies on PBT TT/PCBM blends have demonstrated the preponderance of fullerene intercalation into the polymer alkyl side groups resulting in bimolecular cocrystals following annealing treatments.^{7,10} PBT TT lattice spacing and paracrystalline disorder in the π -stacking direction increase with fullerene intercalation that is marked by broadening in X-ray diffraction peaks and increased amounts of the gauche alkyl side group conformation.⁵

The PBT TT/PCBM system has proven a useful model for predicting optimal blend stoichiometries and morphologies, however, solar cell power conversion efficiencies are <3%,^{11,12} well below current benchmarks.^{13–15} This result is surprising considering the relatively high charge mobilities of pristine PBT TT (>0.001 cm²/V·s at low charge densities),^{16–20} yet it underscores the need to better understand how ground state structure and interactions influence excited state photophysical

Scheme 1. PBT TT (left) and PCBM (right) Structures



processes.²¹ Ultrafast pump–probe transient absorption spectroscopy (TAS) of PBT TT/PCBM blends show evidence of charge separation on time scales <1 ps followed by efficient geminate recombination of separated charge carriers occurring on time scales of ~200 ps.²² These results are consistent with a well-mixed phase favoring efficient charge generation but separated carriers lack sufficient transport pathways and cannot escape Coulomb attractions thus recombining on fast time scales.^{22,23} Importantly, X-ray spectromicroscopy studies of PBT TT/PCBM blends produced estimates of acceptor miscibility of 42 wt %⁹ implying that TAS dynamics are dominated by a well-mixed phase but it is difficult to determine if this corresponds solely to bimolecular crystals. Furthermore, spectroscopic and charge transport studies have shown evidence of structurally similar PBT TT conformational

Received: April 8, 2014

Revised: July 15, 2014

Published: July 18, 2014



polymorphs (conformers) with energy differences of ~ 0.1 eV.^{24,25} PCBM intercalation is expected to disrupt PBTTT conformation and packing in blends but connecting specific ground state structures and interactions to the outcomes of excited state photovoltaic processes remains more elusive.

Here, we use resonance Raman spectroscopy to identify signatures of structurally distinct PBTTT conformers in PCBM blends and track their evolution by varying processing conditions, composition and excitation energies. Resonance Raman and photocurrent imaging are then used to spatially map and correlate their contributions to local material performance in model PBTTT/PCBM solar cells. We show that the PBTTT alkyl-thiophene symmetric C=C stretching vibration (~ 1490 – 1500 cm $^{-1}$) can be decomposed into contributions from ordered (lower energy, $\hbar\omega_{C=C} = 1489$ cm $^{-1}$) and disordered (higher energy, $\hbar\omega_{C=C} = 1500$ cm $^{-1}$) PBTTT conformers which are not evident in optical spectra. We propose that both ordered and disordered PBTTT species are well-mixed with PCBM but only the former exist only in the bimolecular crystal phase. Density functional theory (DFT) Raman simulations and excitation energy dependent Raman spectra indicate that ordering of alkyl-thiophene rings defines the two observed PBTTT forms and the relative amounts of each are determined by the PCBM loading and film processing conditions. Raman excitation profiles further demonstrate that annealing converts the disordered form to bimolecular crystals suggesting that it is in fact a precursor kinetic phase. Well-resolved overtone and combination transition intensities (up to 4 quanta) – chiefly involving the dominant PBTTT CC symmetric skeletal vibrations (~ 1400 – 1600 cm $^{-1}$) – are also apparent and intensities show much smaller sensitivity to PCBM loading indicating PBTTT excitations are electronically localized for both species.

Raman images demonstrate that a significant fraction of ordered PBTTT chains reside in PCBM-rich regions confirming these are indeed bimolecular crystals. However, corresponding photocurrent images show substantial losses in these regions, likely due to efficient geminate charge recombination. Intensity modulated photocurrent spectroscopy (IMPS) measurements of annealed PBTTT/PCBM devices also display positive phase shifts at low modulation frequencies (i.e., photocurrent leads the modulation frequency), which is a signature of nongeminate charge recombination becoming operative.^{26,27} IMPS images of these model PBTTT/PCBM solar cells reveal that this process is most prevalent at boundaries of ordered/disordered PBTTT and PCBM aggregates.

2. METHODS

2.a. Materials and Spectroscopic Characterization. The C₁₄ variant of PBTTT (Aldrich, Mw=49 kDa, PDI = 2.3) and PCBM (Aldrich) were dissolved separately in anhydrous o-dichlorobenzene (5 and 20 mg/mL, respectively) inside a nitrogen circulating glovebox. Samples were heated (100 °C) and stirred for over 8 h to facilitate dissolution and filtered prior to deposition. Blend thin films were produced by adding PCBM and PBTTT solutions in varying weight/weight fractions, i.e., 1:1 up to 1:8 (PBTTT/PCBM) and spin-casting at speeds of 600 rpm for 120s onto rigorously cleaned glass coverslips. Blend solutions were prepared and used immediately after heating to avoid precipitate formation or gelling. Optical absorption spectra of solutions and thin films were recorded on a UV-vis/NIR instrument (Hitachi U4100) and Raman spectra were measured on a home-built scanning microscope spectrometer system described in detail previously.^{28,29} Argon- and krypton-ion laser sources ($\lambda_{exc} = 458$ –

647 nm; 2.71–1.92 eV) as well as a NIR laser diode ($\lambda_{exc} = 785$ nm, 1.58 eV) were used to selectively excite PBTTT in PCBM blends. Single molecule images and spectra of PBTTT diluted into a polystyrene host matrix were also measured using the above confocal microscope with single photon counting techniques. Scattered excitation light was removed by Rayleigh rejection filters (Semrock) prior to entering the polychromator/CCD detector system (Andor). Relative Raman intensity profiles were constructed from comparing excitation energy-dependent Raman spectra and comparing to an in situ external sapphire standard. All spectra were corrected for instrument responses using established methods.³⁰

2.b. Solar Cell Model Device Fabrication and Imaging. Model PBTTT/PCBM solar cells were fabricated using the optimal loading ratio reported in the literature ($\sim 1:4$ w/w)¹¹ and were spun on top of PEDOT:PSS (Baytron) coated indium–tin oxide (ITO) substrates (Metavac) that had previously been heated to 150 °C for 30 min to evaporate residual water. Aluminum was next deposited on top of the PBTTT/PCBM blend under high vacuum to complete the device and current–voltage (*I*–*V*) characterization was carried out in the glovebox in the dark and under AM1.5 illumination (Newport). Typical device power conversion efficiencies were <1% due to nonoptimized morphologies. Resonance Raman spectroscopic- and photocurrent imaging was performed on as-cast and annealed PBTTT/PCBM devices using the above-mentioned Raman imaging spectrometer. PBTTT/PCBM films were annealed for ~ 30 min at 110 °C prior to aluminum deposition in order to generate sufficient phase separation affording better contrast in Raman and photocurrent images. Devices were studied within a home-built inert gas flow cell and no evidence of material or device degradation was observed in the course of spectral image acquisition or in subsequent images collected over the same scan area. Quasi-DC photocurrent imaging was initially performed by modulating the laser excitation (~ 100 – 200 Hz) using a mechanical chopper and current was detected using a lock-in amplifier. Photocurrent images were generated using substantially lower excitation intensities than Raman images (i.e., ~ 10 W/cm 2 vs ~ 1 kW/cm 2 , respectively) to avoid nonlinear effects, such as exciton–exciton annihilation or other photon-induced bimolecular processes and Raman images were constructed using a procedure described previously.²⁸ IMPS spectra and images were next recorded using a laser diode source ($\lambda_{exc} = 488$ nm, Omicron Phox) modulated by the reference output of the phase-sensitive detector and the frequency was swept in the range of ~ 1 Hz up to 20 kHz. Modulation depths were $\sim 10\%$ or slightly less to ensure linear response over the entire frequency range. Ensemble IMPS spectra were measured in a widefield configuration whereas IMPS images were acquired in a confocal geometry and the modulation frequency was held constant over the entire imaging scan. A silicon photodiode with a known frequency response was used as a reference for all IMPS experiments. All photocurrent spectra or images were generated under short-circuit conditions.

2.c. Theoretical Simulations. Raman spectra of a model PBTTT monomer were calculated at the B3LYP/Def-2SV(d) level of theory using the ORCA computational suite. The C₁₄ side groups were replaced with ethyl (C₂) groups and a fully planar BTTT-C₂ monomer and a twisted local minima variant in which the center fused ring is rotated with respect to the two thiophene rings by 29 degrees were simulated.³¹ Resolution of identity (RI-J) and chain of spheres (COSX)³² approximations were utilized with the equivalent quality auxiliary basis set. Atom pairwise dispersion corrections³³ with Becke–Johnson dampening³⁴ were employed.

3. RESULTS AND DISCUSSION

3.a. Optical and Raman Spectroscopy. In general, conjugated polymers become more disordered as fullerene loading increases due to disruption of packing arrangements and reduced planarity between monomers.^{28,35} In crystalline polymers, such as the archetype poly(3-hexylthiophene) (P3HT) system, addition of PCBM breaks up π -stacked lamellar chains in aggregates leading to increases in a solution-

like amorphous component with higher energy and featureless absorption lineshapes.^{36,37} The ability of PCBM to intercalate into PBT TT chains presents an intriguing case challenging traditional views of order/disorder transitions. Spectroscopic and electrical imaging approaches are used here to (i) identify spectroscopic markers of intercalated PBT TT chains in PCBM blends, (ii) assess how ground state structures and interactions affect excited state processes, and (iii) spatially correlate local composition and order/disorder characteristics to material performance in functioning solar cells.

We begin by re-examining the effect of variable PCBM content in PBT TT blend thin film absorption spectra which will be useful later for selection of resonance Raman excitation schemes (*vide infra*). Figure 1 displays as-cast (solid traces) and

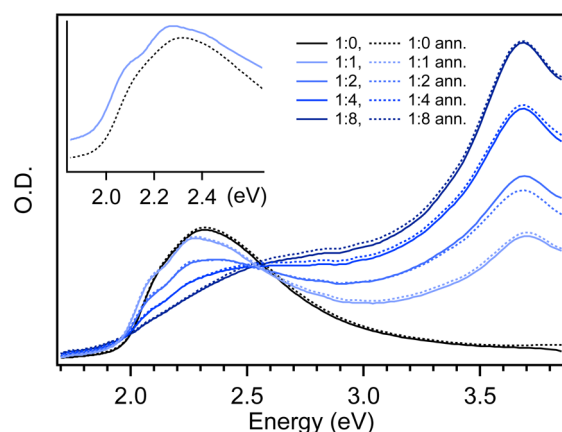


Figure 1. Optical absorption spectra of as-cast (solid traces) and annealed (dotted traces) PBT TT/PCBM blend thin films at several PCBM loadings. Inset: comparison of pristine PBT TT and a 1:2 w/w PCBM blend (offset for clarity).

annealed at 140 °C for 20 min (dotted traces) PBT TT/PCBM blend thin films with 1:1, 1:2, 1:4, and 1:8 w/w ratios deposited on clean glass substrates. Improved resolution of vibronic structure near the PBT TT absorption onset is observed in addition to a slight red-shift (~0.04 eV) relative to the pristine PBT TT line shape (see Figure 1 inset). As PCBM loading increases, the PBT TT contribution decreases concomitantly with an increase of a broad and overlapping higher energy component consistent with the PCBM absorption line shape. Spectra from annealed blends show relatively small changes compared to as-cast films suggesting that conversion from a kinetic mixed (as-cast) phase to the bimolecular crystal phase is not as efficient as reported previously for higher annealing temperatures (i.e., approaching the liquid crystalline transition of PBT TT).

PBT TT/PCBM blend absorption spectra in Figure 1 generally resemble previously published spectra in the singlet exciton onset region^{10,11} but differ from other reports that show better resolution of vibronic structure. This improvement of vibronic resolution upon PCBM addition and annealing has been attributed to bimolecular crystal formation. However, Gasperini and Sivula also recently showed that higher molecular weight PBT TT (>40 kDa) leads to entanglement of chains and rougher film textures that may inhibit bimolecular crystal formation in PCBM blends for larger PBT TT molecular weight fractions in our samples.³⁸ Single-molecule images and spectra of PBT TT diluted into a polystyrene host matrix were also recorded to verify if PBT TT chains were preassociating in

solution prior to blending with PCBM, which might also inhibit bimolecular crystal formation. Images show well-isolated, diffraction-limited spots and areal densities scale linearly with concentration (see Supporting Information) demonstrating that no agglomeration or gelling occurs in our concentration range. We expect that incomplete conversion of a well-mixed, kinetic PBT TT/PCBM phase into bimolecular crystals may arise in films with larger PBT TT molecular weight and polydispersity. However, this feature is advantageous for our study because the range of accessible PBT TT conformations upon PCBM intercalation can be tracked and correlated with their performance attributes.

Evidence of adverse intercalation-induced disorder effects on electrical properties in PBT TT/PCBM blends manifest as over an order of magnitude decrease of charge mobilities.^{11,39} This dramatic decrease in mobility is believed to originate from twisted PBT TT backbones and side group disorder due to intercalated fullerenes. Solid-state NMR studies of PBT TT/PCBM blends support this view and found that ¹³C and ¹H signals from the less-ordered gauche alkyl side group conformer, a minority species in pristine PBT TT (<10%), increase with PCBM loading.⁵ Likewise, a Franck–Condon analysis of pristine PBT TT absorption lineshapes showed evidence of two distinct transitions with electronic origin transitions separated by ~0.1 eV.²⁴ The relatively small difference in energy between apparent intrinsic PBT TT structures potentially complicates the use of absorptive spectroscopies for quantifying amounts and properties of these species since lineshapes strongly overlap and become even more congested in PCBM blends. Resonance Raman spectroscopy can help overcome these issues using selective resonant excitation schemes to target specific electronic excited states corresponding to distinct PCBM intercalation-dependent PBT TT conformers.

Figure 2 presents representative resonance Raman spectra of PBT TT/PCBM blend thin films excited with 514.5 nm (2.41

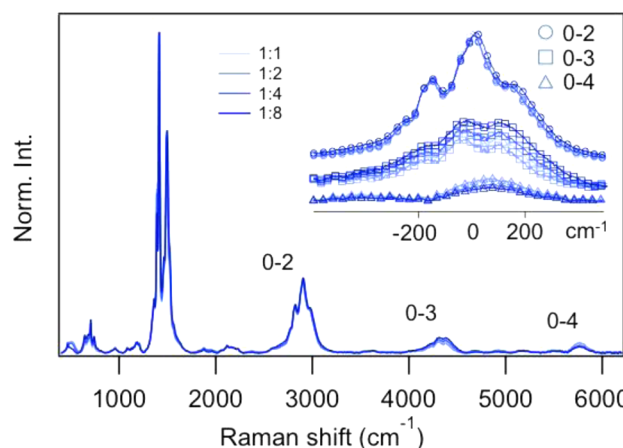


Figure 2. Resonance Raman spectra of PBT TT/PCBM blend thin films (excitation energy = 2.41 eV) with overtone/combination band transitions highlighted and shifted to the most intense transition (inset).

eV) light corresponding to the maximum of the PBT TT absorption line shape. Resonance excitation usually leads to large enhancements (~1 × 10⁵ to 1 × 10¹⁰) in Raman scattering cross sections of the resonant chromophore. Contributions from PCBM in the excitation wavelength range

used are absent demonstrating that PBT TT Raman cross-section enhancements overwhelm those of PCBM despite that it is usually present in larger concentrations (e.g., >1:1 w/w). Well-resolved progressions of overtone and combination bands, mainly involving vibrations of PBT TT C–C and C=C stretching character (see Table 1), are visible. Comparison to

Table 1. Assignments of Main Backbone Raman Bands from PBT TT/PCBM Blends in the Fundamental (0-1) and First Overtone (0-2) Regions

peak	frequency (cm ⁻¹)	assignment
ν_1	1340	
ν_2	1365	
ν_3	1391	thiophene C–C stretch ^a
ν_4	1415	thienothiophene C=C stretch ^a
ν_5	1467	inter-ring thiophene C–C stretch ^a
ν_6	1489	thiophene C=C stretch ^a
ν_7	1500	
ν_8	1523	
ν_9	1563	
	2771	$2\nu_3$
	2804	$\nu_3 + \nu_4$
	2831	$2\nu_4$
	2876	$\nu_4 + \nu_5$
	2908	$\nu_4 + \nu_6$
	2934	$2\nu_5$
	2977	$2\nu_6; \nu_5 + \nu_7$
	3013	$\nu_6 + \nu_8$

^aDetermined from DFT simulations (see below) and ref.⁴⁰

IR absorption spectra of PBT TT/PCBM blends in the first overtone/combination band region (0–2) as well as the appearance of higher order progressions confirm these are not fundamentals of high frequency modes (i.e., C–H stretches).⁵ Table 1 lists mode assignments of both fundamental and overtone/combination bands (for only the 0–2 region).

From Figure 2, we note that only the C–C and C=C symmetric stretches of the thiophene and thienothiophene backbone rings display pure overtone transitions. Higher-order (>0–2) overtone/combination band clusters show greater broadening, probably because of dispersion effects (i.e., wavepacket broadening) due to coupling between nuclear motions. Weak clusters of combination bands from multiple low frequency vibrations, likely from thiophene-thienothiophene ring bends and librations, are also apparent before the 0–2 region (~1700–2500 cm⁻¹). The appearance of multiple apparent progression-forming modes suggests that vibrational displacements are large (i.e., large Huang–Rhys factors, $S = \sum_i^n 1/2\Delta_i^2$, where Δ_i is the displacement for mode i). However, PBT TT absorption band line widths (fwhm) are not significantly different than P3HT or other crystalline polymers ($S \approx 1.0$)⁴¹ meaning that the total vibrational displacements are probably similar. Raman lineshapes in Figure 2 also offer useful insights into PBT TT absorption features. Namely, the weakly resolved vibronic interval can be explained by the Franck–Condon displacement of multiple low frequency modes causing the “valleys” between dominant mode progressions (i.e., the PBT TT CC backbone symmetric stretches, ν_{3-7}) to become filled in. Conversely, increased inhomogeneous broadening might also explain larger absorption vibronic line widths in pristine PBT TT, however, narrowing of line widths in PCBM blends suggests increased order or longer excited state lifetimes.

The latter effect is not expected due to the presence of intimately mixed PCBM electron acceptors. It is also useful to point out that overtone/combination band intensities show less sensitivity with increased PCBM loading (constant excitation energy) implying that either disorder effects are not important until longer times (several vibrational periods, >100 fs) or chromophores are spatially localized making them less sensitive to disorder. Typically, in large molecules with many displaced modes, overtone/combination intensities are usually extinguished before the first overtone (0–2) region because of destructive interference caused by rapid damping from strong coupling to the bath or among chromophores of different energies (inhomogeneous broadening).⁴² This effect appears suppressed in PBT TT systems and we speculate the persistence of the multimode overtone/combination band transitions in PBT TT/PCBM blend Raman spectra arises from weak coupling to the phonon bath and small contributions from inhomogeneous broadening effects.

3.b. Identifying Ordered and Disordered PBT TT Conformers.

The qualitative picture emerging from Raman trends reported in Figure 2 is that the multidimensional excited state wavepacket survives for longer times allowing sufficient buildup of overlap and overtone/combination intensities. This scenario is most consistent with localized excitations despite the relatively high order of PBT TT (even in PCBM blends) that intuitively suggest delocalized electronic structures. The implications of localization/delocalization in polymeric solar cells are significant and have been the subject of recent investigations of ultrafast charge separation.^{43–46} For example, Jamieson et al. highlighted the importance of fullerene crystallites in promoting charge separation while simultaneously suppressing geminate recombination in several polymer/fullerene systems that show varying degrees of mixing.⁴⁶ We consider these aspects for interpreting Raman/photocurrent images in the following.

Further insights into the nature of PBT TT chromophores PBT TT/PCBM blends can be obtained from resonance Raman spectra as a function of excitation energy spanning the PBT TT optical absorption line shape (~1.9–2.7 eV). Figure 3 displays variable excitation energy Raman spectra and are normalized to the thienothiophene ring C=C symmetric stretch (1415 cm⁻¹ mode, ν_4) for comparison. Raman patterns show significant changes with excitation energy consistent with resonant excitation of distinct PBT TT chromophores. In the 0–1 region, the relative intensity of the 1391 cm⁻¹ mode (thiophene symmetric C–C stretching character) decreases and the ~1489–1500 cm⁻¹ band region of the symmetric C=C thiophene ring stretch gains in intensity in addition to apparent blue-shifting and broadening with increased excitation energies. Comparison of the two PCBM loadings also demonstrates specific interactions with PBT TT backbones. For example, a large increase in relative intensity is observed for the ~1489–1500 cm⁻¹ mode in the 1:4 blend for excitation near the PBT TT resolved absorption onset (1.92 eV), suggestive of bimolecular crystals.

Chromophore-specific resonance enhancement is more obvious in the first overtone (0–2) region where increasing excitation energy causes intensity redistributions toward higher frequencies. Residual fluorescence masks overtone/combination bands in the background noise at the lowest excitation energy (647 nm, 1.92 eV) and these spectra were not included. For comparison, we measured Raman spectra of pristine PBT TT and as-cast 1:1 w/w PBT TT/PCBM thin films under

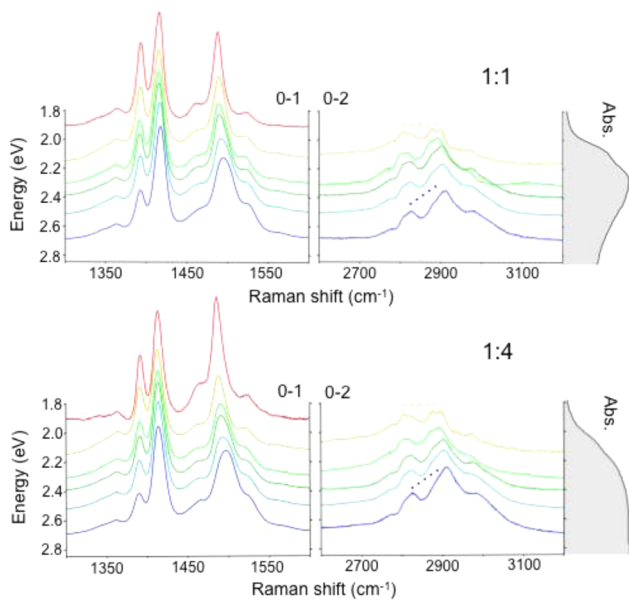


Figure 3. PBTTT/PCBM (1:1 and 1:4 w/w loadings) resonance Raman spectra as a function of variable excitation energies displayed in the fundamental (0–1) and first overtone (0–2) regions of the main PBTTT backbone stretching modes. Corresponding optical absorption spectra are shown and dotted lines indicate changes in 0–2 intensity distributions.

nonresonant conditions ($\lambda_{\text{exc}} = 785 \text{ nm}$, 1.58 eV), that show pronounced red-shifts of the main PBTTT skeletal stretching vibrations for the blend (see the Supporting Information). It is likely that nascent bimolecular crystals in the blend become preresonant at this excitation energy, which also gives rise to very weak overtone transitions.

We propose that line shape (intensity) changes with excitation energy reflect the presence of both ordered and disordered PBTTT conformations whose populations are modulated by PCBM loading and annealing. Raman excitation profiles (REPs) are now constructed to test this hypothesis that reveal vibrational mode-specific views of the excited state potential energy landscape. Figure 4 shows REPs from as-cast PBTTT/PCBM films (solid traces) for all backbone skeletal vibrations showing appreciable intensity in resonance Raman spectra in Figures 2 and 3 (ν_{3-7}) and intensities are reported relative to a nonabsorbing external standard (i.e., sapphire). Generally, REPs bear similarity to absorption lineshapes provided that Raman and absorption transitions involve only a single excited state (i.e., single absorber). REP lineshapes in Figure 4 show noticeable deviations from one-photon absorption spectra (Figure 1) confirming contributions from multiple states. In particular, a pronounced dip around $\sim 2.35 \text{ eV}$ is observed as well as increased activity (cross sections) in the higher energy region of the main PBTTT absorption line shape. As PCBM concentration increases, the relative intensities of the lower energy feature decrease for all mode-specific REPs reported. The dip at 2.35 eV probably results from the crossing of excited state potential energy surfaces of two states leading to destructive quantum interference and intensity de-enhancements.⁴⁷

On the basis of the trends observed here and from previous studies, it is relatively straightforward to assign the low (high) energy REP feature to ordered (disordered) PBTTT chains. Because of the amounts of PCBM used, PBTTT should always

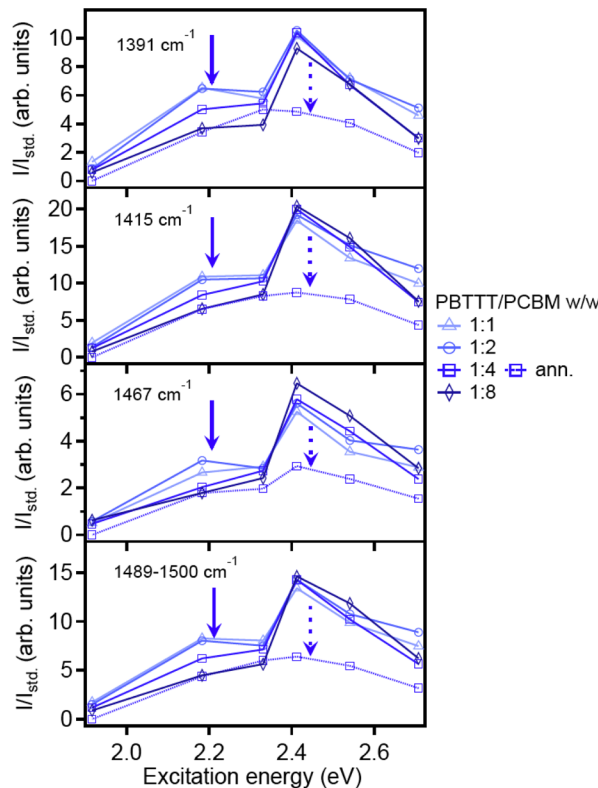


Figure 4. Raman excitation profiles (REPs) of the PBTTT backbone symmetric stretching fundamental (0–1) region from variable PBTTT/PCBM loadings.

exist in a mixed phase owing to large cohesive energy densities between these molecules and available intercalation sites.^{3,48} We next measured REPs of an annealed 1:4 w/w PBTTT/PCBM blend (dotted traces, Figure 4) and compare these to as-cast REP lineshapes. A pronounced decrease of the higher energy REP component is apparent indicating conversion to PBTTT chains with improved backbone and side group order consistent with intercalated bimolecular crystals. This result highlights the greater sensitivity of Raman techniques to chromophore environments compared to one-photon absorption spectroscopy (Figure 1), which can obscure contributions from closely overlapping states.

We now focus on the ~ 1489 – 1500 cm^{-1} region assigned to the C=C symmetric stretch of the thiophene rings ($\nu_{6,7}$, Table 1) that are particularly sensitive to PCBM loading and excitation energy (Figure 3). Figure 5a presents resonance Raman spectra generated from a PBTTT/PCBM blend thin film of a 1:2 w/w ratio in the thiophene C=C symmetric stretching fundamental region. Excitation at the PBTTT red absorption onset (i.e., 1.92 eV) selects the 1489 cm^{-1} (ν_6) component that subsequently blue-shifts and coalesces into the $\sim 1500 \text{ cm}^{-1}$ mode (ν_7) at higher excitation energies (i.e., 2.71 eV). These trends have been explained previously from theoretical studies of oligothiophenes where lower energy chromophores (viz. longer conjugation lengths) show red-shifted Raman-active backbone vibrations.⁴⁹ The 1500 cm^{-1} mode is proposed to originate from disordered PBTTT C=C thiophene rings, probably because of fullerene intercalation-induced disorder among the alkyl side groups causing twisting of the backbone thiophene rings and greater paracrystalline disorder. Likewise, the 1489 cm^{-1} component of the symmetric thiophene C=C stretch derives intensity from ordered PBTTT

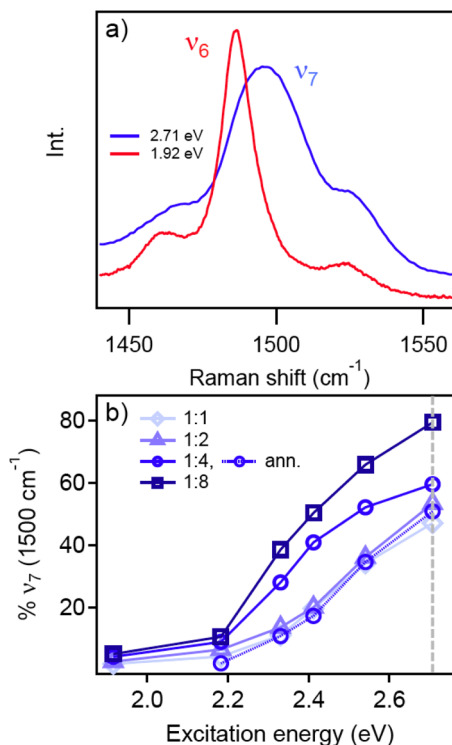


Figure 5. (a) Resonance Raman spectra of as-cast PBT/PCBM blend thin films (1:2 w/w) showing lineshapes of the two distinct PBT forms; ordered (ν_6) and disordered (ν_7) PBT chains. (b) Percent of disordered species present in all blend ratios as a function of excitation energy. The dashed line represents the resonance maximum excitation energy of the disordered form (2.71 eV).

chains in bimolecular crystals, where side group and backbone order is improved. Line widths of both PBT/C thiophene forms are also consistent with their proposed structural origins, namely, ordered conformers are $\sim 15\text{ cm}^{-1}$ compared to $\sim 25\text{ cm}^{-1}$ for disordered chains because of heterogeneity. This feature is also consistent with improved vibronic resolution in absorption spectra of PBT/PCBM blends, which indicates the presence of ordered PBT chains in bimolecular crystals. The relative amounts of ordered and disordered PBT conformers are estimated by deconvoluting the C=C thiophene band using two line shape functions corresponding to the ν_6 and ν_7 bands (Table 1). We do not attempt to obtain absolute cross sections for each species but it is expected that these values are similar because of the structural similarity of ordered and disordered forms (i.e., energy difference of $\sim 0.1\text{ eV}$ or less), which is much subtler than in other crystalline polymers displaying polymorphic behavior, such as P3HT. In this description, the total C=C thiophene Raman band intensity is a linear combination of both components and we use this simple model to assess how the amounts of disordered PBT conformers, $((I_7)/(I_6+I_7))$, change with blend film processing conditions. We further speculate that the disordered component is the precursor species to the ordered PBT form in bimolecular crystals and the evolution of both forms can be revealed from Raman spectra as a function of varying PCBM loading and excitation energy. Figure 5b presents estimates of the disordered PBT content in as-cast blends, which increases with PCBM content and excitation energies. For comparison, $((I_7)/(I_6+I_7))$ values were determined for an annealed blend (1:4 w/w) and

displayed in Figure 5b, which has significantly less of the disordered PBT because of conversion into bimolecular crystals which is consistent with REP trends in Figure 4 and corresponding plots of $(I_7)/(I_6+I_7)$ values confirm this behavior (not shown).

3.c. Theoretical Raman Simulations. DFT Raman simulations of a planar and twisted PBT model monomer system (BTTT-C₂) are next performed to validate our proposed model and are shown in Figure 6 with their

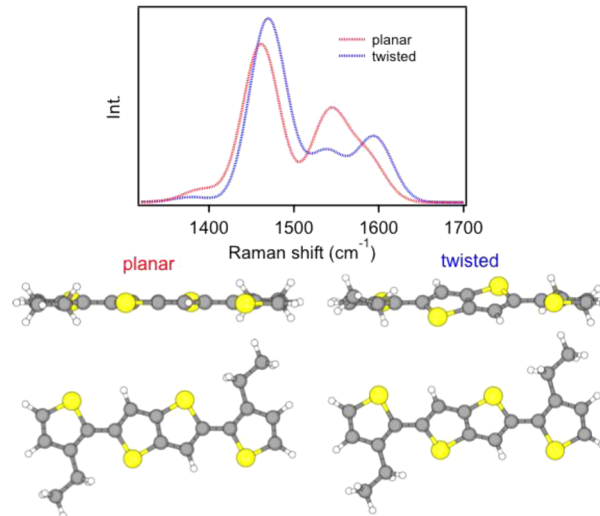


Figure 6. Simulated Raman spectra of the BTTT-C₂ monomer and structures.

respective structures. Calculated DFT Raman line shape trends agree very well with experiment although nonresonant conditions are used in simulations and a scaling factor of 0.95 must be applied to calculated frequencies in order to compare with experiment. The nominal C–C symmetric stretch appearing at 1461 cm⁻¹ for the planar conformation undergoes a blue shift of $\sim 7\text{ cm}^{-1}$ in the twisted variant. Most notably, intensity redistributions occur between the inter-ring C=C symmetric stretch (1541 cm⁻¹) and the thiophene C=C stretch (1594 cm⁻¹) depending on backbone planarity. For example, the latter increase in intensity for the twisted BTTT-C₂ variant whereas the former dominate in the planar monomer. Previous DFT simulations of planar and twisted PBT trimer structures show similar trends as presented in Figure 6⁴⁰ confirming that at least two PBT types are present in PCBM blends revealed from PCBM loading- and excitation energy dependent Raman spectra. Moreover, calculated frequencies and intensities of trimers were very similar to experimental Raman spectra, suggesting that excitations are probably localized to a few monomer units.

Thus far we have shown that the ability of the two species model to decompose key Raman bands into separate contributions from morphology-dependent PBT conformers offers a much simpler means to assess order/disorder transitions in this system. Although DFT simulations predict observed experimental behavior, they do not allow us to incorporate side group disorder and paracrystallinity. It is also important to note that ordered PBT chains in bimolecular crystals are twisted but side group disorder should be diminished relative to the kinetic disordered intercalated form.

3.d. Spatially Mapping Order–Disorder and Photocurrent Generation in Solar Cells. Despite the relatively poor performance of PBT/PCBM, we have thus far demonstrated its value as a model for understanding donor/acceptor interactions and supramolecular organization and their impact material performance. Resonance Raman spectroscopic and photocurrent imaging techniques are now employed to spatially resolve how ordered and disordered PBT chains impact local device performance in model solar cell devices. For these experiments, as-cast and annealed PBT/PCBM blends in 1:4 w/w ratios (the optimal blend ratio reported for solar cells)^{16,17} were prepared to compare morphology-dependent order/disorder spatial distributions. Because these studies emphasize model PBT/PCBM morphologies, power conversion efficiencies were <1% but nonetheless show good stability and expected diode-like behavior (see the Supporting Information). We emphasize annealed devices because of better material performance in addition to better contrast in Raman and photocurrent images.

Figure 7 shows representative resonance Raman and photocurrent images of a 1:4 w/w annealed device and

the $\nu_{6,7}$ modes and corresponding photocurrent over the same area is shown in Figure 6b. Lower PBT intensity represents PCBM-rich areas, but an appreciable amount of PBT still exists in these regions indicating these are most likely bimolecular crystals. Because the PCBM loading of these devices is high (1:4 w/w), it is unlikely that PBT completely phase separates meaning the entire film corresponds to ordered and disordered mixed phases. Photocurrent images (Figure 7b) show much lower output in putative bimolecular crystal regions probably originating from unbalanced charge transport as expected from increased charge recombination.^{52,53}

The PBT thiophene C=C stretch is now decomposed into its constituent components and Figures 7c,d shows fractional compositions of ordered ($(I_6)/(I_6+I_7)$) and disordered ($(I_7)/(I_6+I_7)$) forms, respectively, using the same procedure described above. Comparison of these images with morphology-dependent frequency dispersion characteristics (Figure 7e, f, respectively) confirm that bimolecular crystals are indeed most concentrated in PCBM-rich regions (i.e., lower PBT intensities, Figure 7a). Although Raman signatures for PCBM are absent, direct excitation may lead to photocurrent from hole transfer to PBT from photoexcited PCBM. We measured photocurrent images on the same devices using 488 nm (2.54 eV) light, which is near the PBT absorption maximum, but identical behavior is observed (see the Supporting Information). The effects of excitation intensity and PCBM crystal size (annealing time) on local photocurrent production were also investigated and no significant differences were found (see Supporting Information). Interestingly, maximum photocurrent generation originates from regions with more disordered PBT content. We speculate that increased geminate charge recombination dominates in bimolecular crystals, which is consistent with previous TAS studies of PBT/PCBM thin films predominantly in the bimolecular crystal phase.

Raman and photocurrent images of as-cast PBT/PCBM (1:4 w/w) devices were also measured under the same conditions as annealed devices (see the Supporting Information). These devices generally show relatively uniform morphological features and photocurrent is at least an order of magnitude smaller than annealed devices when illuminating with a diffraction-limited laser spot.

Resonance Raman and photocurrent images have so far demonstrated that morphology-dependent variations in material performance are determined not only from the type and amounts of PBT species but also their spatial distributions in the device active layer. Intensity modulated photocurrent spectroscopy (IMPS) and imaging is next used to expose how specific conformers and morphologies impact loss mechanisms in PBT/PCBM devices, namely, charge recombination.

IMPS uses a small (~10%) sinusoidal modulation of the excitation source and the frequency is swept over several decades (typically, ~0.1 Hz up to ~1 MHz). Figure 8 shows IMPS ensemble spectra from annealed (Figure 8a, c) and as-cast (Figure 8b, d) PBT/PCBM (1:4 w/w) solar cells recorded by using a widefield configuration that illuminates the entire device active area (~20 mm²). Ensemble IMPS sweeps show similar behavior as reported previously in related polymer/fullerene solar cells and a characteristic maximum is observed in photocurrent sweeps and the phase decreases significantly in this region toward its maximum (~−180°). Photocurrents in the low frequency regime (<1 kHz) are almost entirely real and phase shifts are positive (<10°) for

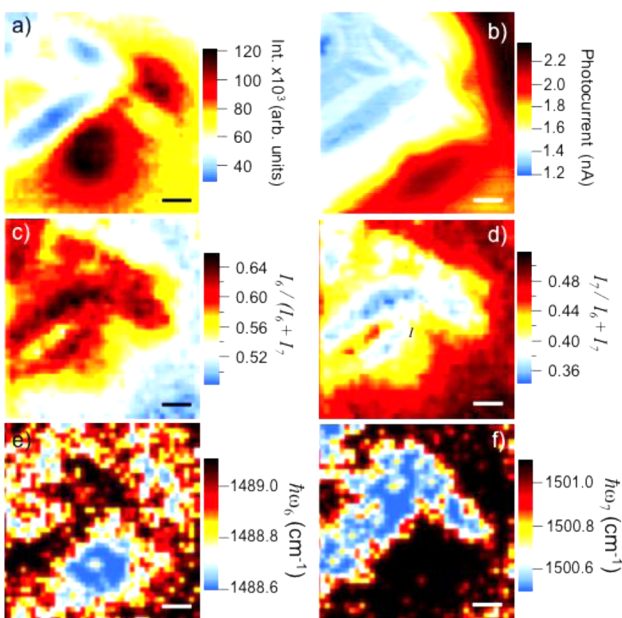


Figure 7. (a) Total integrated Raman intensity of C=C symmetric stretching mode ($\nu_{6,7}$) and (b) corresponding photocurrent images of annealed PBT/PCBM (1:4 w/w) device (excitation energy = 2.71 eV). (c, d) Ratios and (e, f) frequency dispersion of ordered (ν_6) and disordered (ν_7) PBT species, respectively. A ± 5% tolerance was applied for determining the center frequencies of each PBT component. Scale bar = 2 μ m.

appreciable microscopic phase segregation is apparent within the active layer. Raman images represent the ~1489–1500 cm^{−1} spectral region of the thiophene C=C stretches and are generated using 458 nm (2.71 eV) excitation light. This excitation energy was specifically chosen to selectively interrogate disordered PBT chains and their spatial locations relative to ordered chains in bimolecular crystals. Because charge transfer and recombination processes are strongly dependent on local polymer ordering and composition we expect significantly different responses for each PBT form.^{50,51} Figure 7a presents the total integrated intensity of

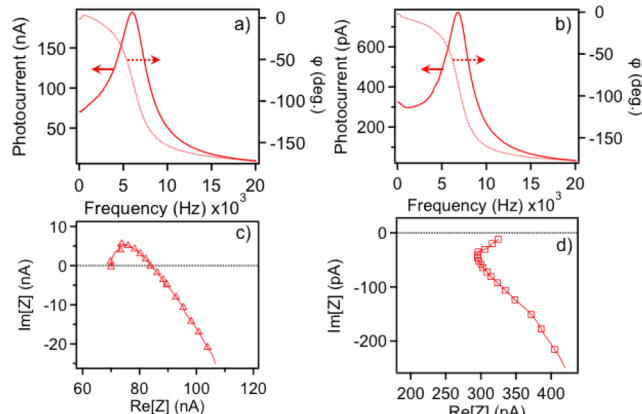


Figure 8. IMPS spectra (photocurrent and phase shift, φ) and Nyquist (complex) plots of (a, c) annealed and (b, d) as-cast PBTTT/PCBM (1:4 w/w) solar cells, respectively.

annealed devices indicating that charge carriers lead the modulation frequency. On the other hand, as-cast films typically show lower photocurrents and phase shifts start at $\sim 0^\circ$. At larger modulation frequencies, both devices show increasingly negative phase shifts due to charge carriers lagging behind the modulation frequency.

Seminikhin and co-workers first reported positive phase shifts at low modulation frequencies or, a component in the first quadrant of the complex (Nyquist) IMPS plot from P3HT/PCBM devices.²⁶ This feature has been attributed to nongeminate charge recombination that becomes more pronounced as the device ages. Luther and co-workers recently advanced this understanding by systematically studying device aging and preparation conditions and tracking IMPS responses.²⁷ These authors showed that first quadrant photocurrent contributions in Nyquist plots, result from the formation of deep traps and introduced a drift-diffusion model to account for this behavior.²⁷ The observation of positive phase shifts in the low-frequency modulation regime demonstrates that nongeminate recombination processes become operative in annealed PBTTT/PCBM devices indicating suppression of prevailing geminate recombination. The lack of this signature in as-cast devices (either fresh or aged) supports this view because geminate processes occur on faster time scales beyond what is currently accessible by IMPS techniques. Nonetheless, our ability to spatially correlate the specific PBTTT phase to local photocurrent production can be leveraged to map recombination sites or zones to morphological boundaries using a hybrid IMPS imaging approach.

IMPS images were generated using the same high NA objective used for Raman and quasi-DC photocurrent images and are shown in Figure 9. Scan ranges were expanded to 20 \times 20 μm and laser modulation frequencies were held fixed throughout the scans using similar power densities as the quasi-DC photocurrent images shown in Figure 7. Several modulation frequencies were selected representing different charge transport and recombination regimes observed in ensemble IMPS spectra, namely, low frequency (e.g., 1 and 3 kHz), near the maximum frequency photocurrent (~ 7 kHz) and at the high-frequency regime (~ 9 kHz). PBTTT/PCBM blends were annealed for longer times in order to achieve greater phase separation that allows us to better resolve distinct phase boundaries. Similar to quasi-DC Raman and photocurrent images shown in Figure 7, bimolecular crystals in Figure

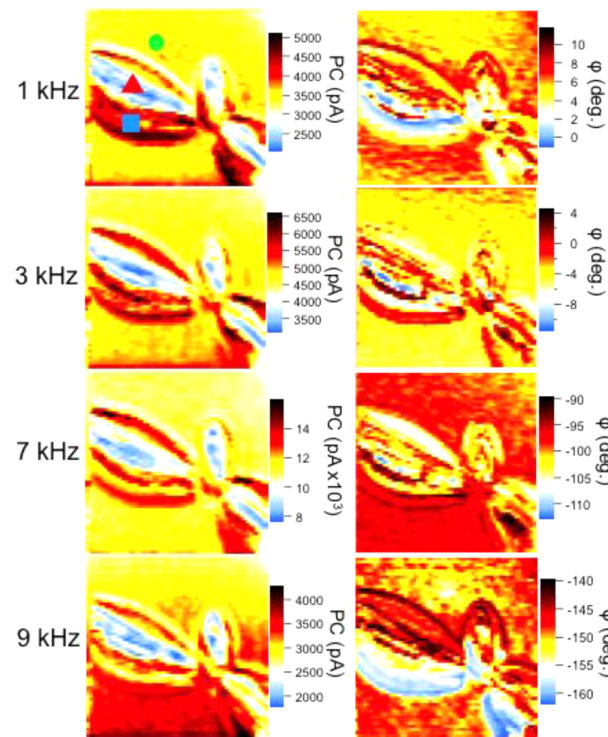
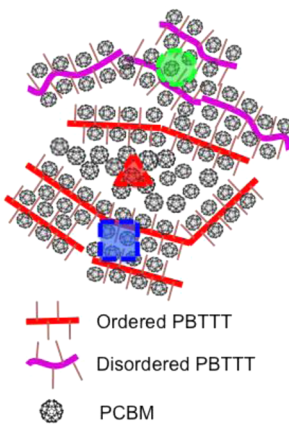


Figure 9. IMPS photocurrent (left) and phase shift (φ , right) images of same area at 1 kHz, 3 kHz, 7 kHz, 9 kHz laser modulation frequency of annealed PBTTT/PCBM (1:4 w/w) device (excitation energy = 2.54 eV). Image scan area = 400 μm^2 .

9 produce lower photocurrent output than the surrounding mixed phase. From the IMPS phase shift (φ) images, positive phase shift accumulates on the periphery of these regions. As the modulation frequency increases past the maximum, IMPS images lose contrast owing to carriers lagging behind the modulation. We infer that boundaries surrounding regions of positive phase shift (or, relative positive phase shift at higher modulation frequencies) represent recombination zones for nongeminate processes since separated electron–hole carriers can diffuse away from the interface before becoming trapped. In this case, trap sites are probably located at phase boundaries between ordered and disordered PBTTT regions, which is consistent with the current and phase maps (Figure 9). Despite loss of resolution at higher modulation frequencies, these results in general show that lateral diffusion effects are probably not significant since features of size scales comparable to the diffraction limit are resolvable.

On the basis of optical and Raman spectra of pristine PBTTT and PCBM blends, small energetic differences between ordered and disordered PBTTT species imply that charge traps are mostly shallow in nature. Troisi and co-workers reported “self-healing” phenomena occur in pristine PBTTT where facile detrapping of charges occurs due to small structural changes ($\sim k_B T$).²⁰ However, greater disorder in blends probably results in deeper traps, which is evident from IMPS results. Although it is unclear if a similar self-healing mechanism is conceivable in PBTTT/PCBM solar cells, effective management of order–disorder boundaries through new molecular-level organization strategies may help overcome detrimental trapping effects.

Scheme 2. Proposed Morphology-Dependent Compositions in PBT/PCBM Films Shown in Figure 9 (see corresponding symbols in 1 kHz current image, top left)



4. CONCLUSIONS

We have shown that resonance Raman spectroscopy of PBT/PCBM blends can be used in a straightforward manner to extract the relative amounts of ordered and disordered PBT/TTT conformers. Both ordered and disordered components exist in a mixed phase but, the former are found in bimolecular crystals whereas the latter correspond to precursors of the ordered forms. The larger frequency and line width of disordered chains likely originate from greater side group disorder and highly twisted monomer thiophene rings due to disordered alkyl side groups. DFT simulations and excitation energy dependent Raman spectra supported this assignment although we point out that previous studies have shown that PBT/TTT chains in the bimolecular crystals also tend to twist around the intercalated fullerene but side group and paracrystalline disorder is reduced. This common structural trait shared between ordered and disordered PBT/TTT chains localizes excitations, hence, the invariance of Raman overtone-combination intensities with PCBM loading. Resonance Raman and photocurrent images next expose the morphology dependence of intercalation-induced order/disorder and its influence on local current generation. IMPS spectra and images showed evidence for increased nongeminate recombination at the boundaries between bimolecular crystals and disordered mixed zones. Overall, these experiments help bridge the gap in understanding of how ground-state structure and acceptor interactions influence the outcomes of excited state photovoltaic processes.

■ ASSOCIATED CONTENT

Supporting Information

Absorption spectra and optical images of PBT/PCBM films under different annealing conditions, examples of resonance Raman spectral fits, photocurrent images of different size PCBM regions and schematics, excitation intensity dependent photocurrent images, single molecule fluorescence images of PBT/TTT. This material is available free of charge via the Internet at <http://pubs.acs.org>.

■ AUTHOR INFORMATION

Corresponding Author

*E-mail: jkgrey@unm.edu.

Notes

The authors declare no competing financial interest.

■ ACKNOWLEDGMENTS

We acknowledge contributions from Eric Martin for assistance with resonance Raman excitation profiles. J.K.G. acknowledges financial support from the National Science Foundation (CHE-0955242 and IIA-1301346).

■ REFERENCES

- Treat, N. D.; Varotto, A.; Takacs, C. J.; Batara, N.; Al-Hashimi, M.; Heeney, M. J.; Heeger, A. J.; Wudl, F.; Hawker, C. J.; Chabinyc, M. L. *J. Am. Chem. Soc.* **2012**, *134*, 15869.
- Collins, B. A.; Gann, E.; Guignard, L.; He, X.; McNeill, C. R.; Ade, H. *J. Phys. Chem. Lett.* **2010**, *1*, 3160.
- Miller, N. C.; Gysel, R.; Miller, C. E.; Verploegen, E.; Bailey, Z.; Heeney, M.; McCulloch, I.; Bao, Z.; Toney, M. F.; McGehee, M. D. *J. Polym. Sci., Part B: Polym. Phys.* **2011**, *49*, 499.
- Miller, N. C.; Sweetnam, S.; Hoke, E. T.; Gysel, R.; Miller, C. E.; Bartelt, J. A.; Xie, X.; Toney, M. F.; McGehee, M. D. *Nano Lett.* **2012**, *12*, 1566.
- Miller, N. C.; Cho, E.; Junk, M. J. N.; Gysel, R.; Risko, C.; Kim, D.; Sweetnam, S.; Miller, C. E.; Richter, L. J.; Kline, R. J.; Heeney, M.; McCulloch, I.; Amassian, A.; Acevedo-Feliz, D.; Knox, C.; Hansen, M. R.; Dudenko, D.; Chmelka, B. F.; Toney, M. F.; Bredas, J.-L.; McGehee, M. D. *Adv. Mater.* **2012**, *24*, 6071.
- Chabinyc, M. L.; Toney, M. F.; Kline, R. J.; McCulloch, I.; Heeney, M. *J. Am. Chem. Soc.* **2007**, *129*, 3226.
- Mayer, A. C.; Toney, M. F.; Scully, S. R.; Rivnay, J.; Brabec, C. J.; Schärber, M.; Koppe, M.; Heeney, M.; McCulloch, I.; McGehee, M. D. *Adv. Funct. Mater.* **2009**, *19*, 1173.
- Cho, E.; Risko, C.; Kim, D.; Gysel, R.; Miller, N. C.; Breiby, D. W.; McGehee, M. D.; Toney, M. F.; Kline, R. J.; Bredas, J.-L. *J. Am. Chem. Soc.* **2012**, *134*, 6177.
- He, X.; Collins, B. A.; Watts, B.; Ade, H.; McNeill, C. R. *Small* **2012**, *8*, 1920.
- Cates, N. C.; Gysel, R.; Bailey, Z.; Miller, C. E.; Toney, M. F.; Heeney, M.; McCulloch, I.; McGehee, M. D. *Nano Lett.* **2009**, *9*, 4153.
- Parmer, J. E.; Mayer, A. C.; Hardin, B. E.; Scully, S. R.; McGehee, M. D.; Heeney, M.; McCulloch, I. *Appl. Phys. Lett.* **2008**, *92*, 113309/1.
- Sun, Q.; Park, K.; Dai, L. *J. Phys. Chem. C* **2009**, *113*, 7892.
- He, F.; Yu, L. *J. Phys. Chem. Lett.* **2011**, *2*, 3102.
- Li, G.; Zhu, R.; Yang, Y. *Nat. Photonics* **2012**, *6*, 153.
- Heeger, A. J. *Adv. Mater.* **2014**, *26*, 10.
- DeLongchamp, D. M.; Kline, R. J.; Jung, Y.; Germack, D. S.; Lin, E. K.; Moad, A. J.; Richter, L. J.; Toney, M. F.; Heeney, M.; McCulloch, I. *ACS Nano* **2009**, *3*, 780.
- Li, J.; Sun, Z.; Yan, F. *Adv. Mater.* **2012**, *24*, 88.
- Poelking, C.; Andrienko, D. *Macromolecules* **2013**, *46*, 8941.
- Poelking, C.; Cho, E.; Malafeev, A.; Ivanov, V.; Kremer, K.; Risko, C.; Bredas, J.-L.; Andrienko, D. *J. Phys. Chem. C* **2013**, *117*, 1633.
- Liu, T.; Troisi, A. *Adv. Funct. Mater.* **2014**, *24*, 925.
- McGehee, M. D.; Topinka, M. A. *Nat. Mater.* **2006**, *5*, 675.
- Hwang, I.-W.; Kim, J. Y.; Cho, S.; Yuen, J.; Coates, N.; Lee, K.; Heeney, M.; McCulloch, I.; Moses, D.; Heeger, A. J. *J. Phys. Chem. C* **2008**, *112*, 7853.
- Banerji, N. *J. Mater. Chem. C* **2013**, *1*, 3052.
- Wang, S.; Tang, J.-C.; Zhao, L.-H.; Png, R.-Q.; Wong, L.-Y.; Chia, P.-J.; Chan, H. S. O.; Ho, P. K. H.; Chua, L.-L. *Appl. Phys. Lett.* **2008**, *93*, 162103/1.
- Rivnay, J.; Noriega, R.; Northrup, J. E.; Kline, R. J.; Toney, M. F.; Salleo, A. *Phys. Rev. B* **2011**, *83*, 121306/1.
- Byers, J. C.; Ballantyne, S.; Rodionov, K.; Mann, A.; Semenikhin, O. A. *ACS Appl. Mater. Interface* **2011**, *3*, 392.
- Set, Y. T.; Heinemann, M. D.; Birgersson, E.; Luther, J. *J. Phys. Chem. C* **2013**, *117*, 7993.

- (28) Gao, Y.; Grey, J. K. *J. Am. Chem. Soc.* **2009**, *131*, 9654.
(29) Gao, Y.; Martin, T. P.; Thomas, A. K.; Grey, J. K. *J. Phys. Chem. Lett.* **2010**, *1*, 178.
(30) Ejder, E. *J. Opt. Soc. Am.* **1969**, *59*, 223.
(31) Neese, F. *WIREs Comput. Mol. Sci.* **2011**, *2*, 73.
(32) Neese, F.; Wennmohs, F.; Hansen, A.; Becker, U. *Chem. Phys.* **2009**, *356*, 98.
(33) Grimme, S.; Ehrlich, S.; Goerigk, L. *J. Comput. Chem.* **2011**, *32*, 1456.
(34) Grimme, S.; Antony, J.; Ehrlich, S.; Krieg, H. *J. Chem. Phys.* **2010**, *132*, 154104/1.
(35) Woo, C. H.; Thompson, B. C.; Kim, B. J.; Toney, M. F.; Frechet, J. M. J. *J. Am. Chem. Soc.* **2008**, *130*, 16324.
(36) Gao, Y.; Martin, T. P.; Niles, E. T.; Wise, A. J.; Thomas, A. K.; Grey, J. K. *J. Phys. Chem. C* **2010**, *114*, 15121.
(37) Clark, J.; Silva, C.; Friend, R. H.; Spano, F. C. *Phys. Rev. Lett.* **2007**, *98*, 206406/1.
(38) Gasperini, A.; Sivula, K. *Macromolecules* **2013**, *46*, 9349.
(39) Lee, M. J.; Gupta, D.; Zhao, N.; Heeney, M.; McCulloch, I.; Sirringhaus, H. *Adv. Funct. Mater.* **2011**, *21*, 932.
(40) Cho, E. Ph.D. thesis, Georgia Institute of Technology, Atlanta, 2012.
(41) Spano, F. C. *Acc. Chem. Res.* **2010**, *43*, 429.
(42) Heller, E. *J. Acc. Chem. Res.* **1981**, *14*, 368.
(43) Gelinas, S.; Rao, A.; Kumar, A.; Smith, S. L.; Chin, A. W.; Clark, J.; van der Poll, T. S.; Bazan, G. C.; Friend, R. H. *Science* **2014**, *343*, 512.
(44) Kaake, L. G.; Jasieniak, J. J.; Bakus, R. C.; Welch, G. C.; Moses, D.; Bazan, G. C.; Heeger, A. J. *J. Am. Chem. Soc.* **2012**, *134*, 19828.
(45) Kaake, L. G.; Moses, D.; Heeger, A. J. *J. Phys. Chem. Lett.* **2013**, *4*, 2264.
(46) Jamieson, F.; Domingo, E. B.; McCarthy-Ward, T.; Heeney, M.; Stingelin, N.; Durrant, J. R. *Chem. Sci.* **2012**, *4*, 2264.
(47) Reber, C.; Zink, J. I. *J. Phys. Chem.* **1992**, *96*, 571.
(48) Miller, N. C.; Cho, E.; Gysel, R.; Risko, C.; Coropceanu, V.; Miller, C. E.; Sweetnam, S.; Sellinger, A.; Heeney, M.; McCulloch, I.; Bredas, J.-L.; Toney, M. F.; McGehee, M. D. *Adv. Energy Mater.* **2012**, *2*, 1208.
(49) Milani, A.; Brambilla, L.; Zoppo, M. D.; Zerbi, G. *J. Phys. Chem. B* **2007**, *111*, 1271.
(50) Vazquez, H.; Troisi, A. *Phys. Rev. B* **2013**, *88*, 205304/1.
(51) Savenije, T. J.; Grzegorczyk, W. J.; Heeney, M.; Tierney, S.; McCulloch, I.; Siebbeles, L. D. A. *J. Phys. Chem. C* **2010**, *114*, 15116.
(52) Dante, M.; Peet, J.; Nguyen, T.-Q. *J. Phys. Chem. C* **2008**, *112*, 7241.
(53) Coffey, D. C.; Reid, O. G.; Rodovsky, D. B.; Bartholomew, G. P.; Ginger, D. S. *Nano Lett.* **2007**, *7*, 738.